Experimental investigation into turbulent negatively buoyant jets using combined PIV and PLIF measurements

L. Milton-McGurk[a,*], N. Williamson[a], S. W. Armfield[a], M. P. Kirkpatrick[a]

[a]*School of Aerospace, Mechanical and Mechatronic Engineering*
The University of Sydney, NSW 2006, Australia

Abstract

Turbulent negatively buoyant jets occur when the buoyancy of a jet opposes its source momentum. In these flows, the fluid will rise until it reaches a stagnation point and a return flow is established, forming a fountain (Hunt and Burridge, 2015). This study looks at both the initial negatively buoyant jet stage of this flow, before the return flow has established, and the fully developed fountain stage. Two-dimensional particle image velocimetry (PIV) and planar laser induced fluorescence (PLIF) are used to simultaneously measure the velocity and scalar concentration fields. An experimental and image processing procedure for the PLIF is introduced that accounts for pulse-to-pulse variations in laser power and beam profile for an Nd:YAG laser, which has been demonstrated to reduce the error in scalar concentration measurements. The flow is investigated experimentally using a 1m^3 tank of salt-water ambient with freshwater+ethanol negatively buoyant jets, allowing for measurements to be taken at $Fr_o = 30$ and $Re_o = 5900$. The entrainment coefficient for a negatively buoyant jet has been estimated as $\alpha \cong 0.054$, lower than a neutral jet at $\alpha \cong 0.058$. A finding consistent with existing literature (Bloomfield and Kerr, 2000; McDougall, 1981).

Keywords: negatively buoyant jet, fountain, PIV, LIF,

*Corresponding author
Email address: lmil3787@sydney.edu.au (L. Milton-McGurk)

1. Introduction

A vertically aligned turbulent round jet with negative buoyancy will rise from its source due to its initial momentum. Opposing buoyancy forces eventually reduce the momentum of the jet to zero where the fluid changes direction and forms an annular return flow. The period prior to the return flow forming will be referred to as the 'negatively buoyant jet' stage. After this initial rise the return flow starts to interact with the upward-flowing fluid, ultimately reducing the initial height of the jet, z_i, to a final 'quasi steady-state' height, z_{ss}, which the flow oscillates around indefinitely. This stage of the flow is distinctly different from the negatively buoyant jet stage, containing 'inner flow' (IF) and 'outer flow' (OF) regions, and will be referred to as the 'fully developed fountain' stage. For high Reynolds numbers, the mean and steady state rise heights are governed by the Froude number,

$$Fr_o = \frac{U_o}{\sqrt{r_o b_o}}, \tag{1}$$

where U_o is the average vertical velocity, r_o is the radius of the inlet and $b_o = g(\rho_o - \rho_a)/\rho_a$ is the buoyancy (with subscript o indicating values are taken at the source). Here ρ_o and ρ_a are the densities of the source and ambient fluid, and g is the gravitational acceleration. It has been shown that for 'highly forced' fountains ($Fr_o \gtrsim 5.5$), the initial and steady state heights follow $z_{ss}/r_o = 2.46Fr_o$ and $z_i = 1.45z_{ss}$ (Burridge and Hunt, 2012).

The classical plume model by Morton, Taylor and Turner (1956), and early work by Priestley and Ball (1955), have underpinned many attempts to model turbulent jets and plumes. These typically use the conservation of mass, momentum and buoyancy equations, coupled with the 'entrainment assumption', to produce integral models to predict the flow. The entrainment assumption states that the the radial velocity, V_e, of entrained fluid moving from the ambient into a plume/jet is proportional to a characteristic vertical velocity at that height, $\hat{U}$ (Morton et al., 1956). The constant of proportionality, the 'entrainment coefficient', is denoted α and is usually assumed to remain constant with

distance from the source. There has been considerable work applying these integral models to neutral/positively buoyant jets and plumes, with estimates in literature for the entrainment coefficient spanning the ranges $0.052 \lesssim \alpha_j \lesssim 0.08$ for pure jets and $0.10 \lesssim \alpha_p \lesssim 0.16$ for pure plumes (Ezzamel et al., 2015; Hussein et al., 1994; van Reeuwijk and Craske, 2015; Carazzo et al., 2006). Here α corresponds to the 'top hat' formulation of the entrainment coefficient, as opposed to the Gaussian formulation, α_G, where $\alpha = \sqrt{2}\alpha_G$. The entrainment coefficient for buoyant jets (forced plumes) varies between these two asymptotic cases (Priestley and Ball, 1955; Fox, 1970). There has been considerably less consensus on the value of α for negatively buoyant jets, with some studies assuming the value for a neutral jet $\alpha \cong 0.085$ (Bloomfield and Kerr, 2000; McDougall, 1981) and other suggesting it may be considerably lower $\alpha \cong 0.057$ (Kaminski et al., 2005; Papanicolaou et al., 2008). The present research uses experimental methods to obtain measurements of the velocity and scalar concentration fields of a negatively buoyant jet and fully developed fountain, and an estimate for the value of α for negatively buoyant jets is presented. The experimental procedure is discussed, including details of an image processing procedure for the PLIF measurements that accounts for variations in the laser power and beam profile between pulses of the Nd:YAG laser.

2. Experiments

The flow was achieved by injecting a mixture of freshwater, ethanol and Rhodamine 6G vertically down into a 1m^3 tank of salt-water. The fluid enters the tank through a round pipe that could be interchanged to obtain a range of diameters from $D = 5$ to 10mm, with entry lengths $\geq 75D$. Ethanol was added to the source mixture in order to achieve the same refractive index as the ambient salt-water, and Rhodamine 6G to act as the fluorescent dye. The source mixture had a lower density than the ambient, and so experienced an opposing buoyancy force when entering the tank vertically from above. The flow rate of the fluid was set by an Ismatic MCP-Z gear pump. Planar laser-induced

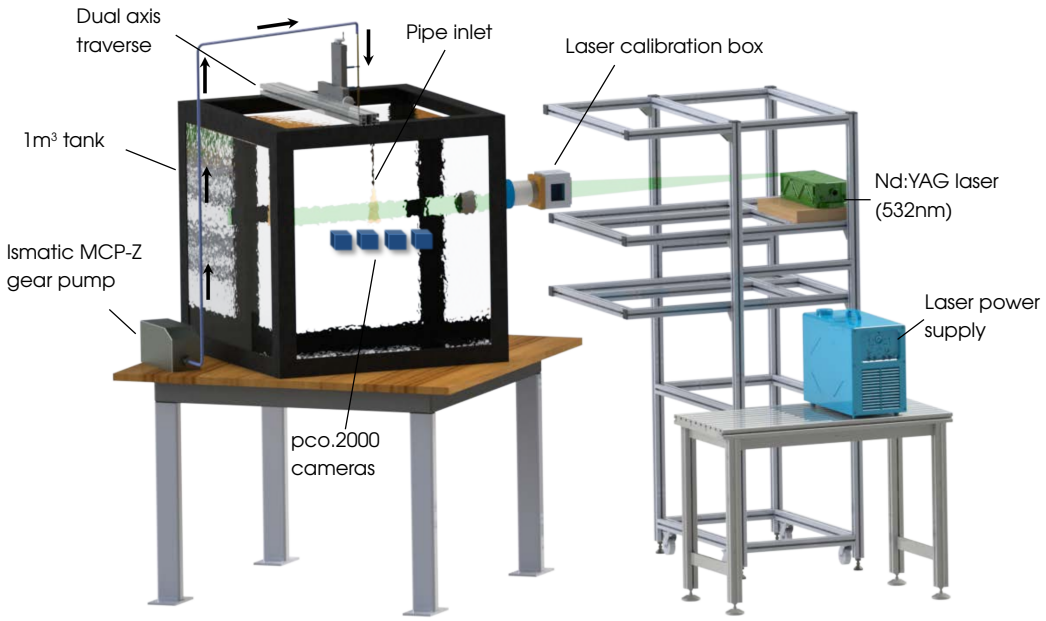

Figure 1: Graphical illustration of the present experimental set-up.

fluorescence (PLIF) and particle image velocimetry (PIV) was used to measure the scalar concentration and velocity fields in the flow, which was captured using four pco.2000 CCD cameras synchronised with a laser pulse using a MotionPro Timing Hub. A double pulsed 145mJ 532nm Evergreen Nd:YAG laser operating at 7Hz was used to generate the beam. This was then shaped into a 63.5mm wide laser sheet using a rectangular and spherical lens pair, which converged the sheet to a thickness of approximately 1mm in the region of interest. A graphical illustration of the experimental set-up is given in figure 1, showing the location of cameras and pipe inlet, and the path and shape of the laser sheet.

3. Particle image velocimetry

A 532 ± 2mm band-pass filter was used on the PIV cameras to filter out ambient light and the Rhodamine 6G fluorescence, but allowing the scattered light from the particles through to the CCD sensor. In preparing the source fluid

mixture, freshwater was taken from the local water supply and passed through a 'degassing' system consisting of a heat exchanger and hot water urn. This heated the water to approximately 70°C, which was sufficient to allow most of the air to escape and thus reduce the prevalence of bubbles in the fluid. There were many natural impurities in the water supply, which were detectable by PIV cameras and appeared as approximately $4 - 10$ pixel ($0.1 - 0.3$mm) particles in the images. These natural particles provided sufficient particle density in the PIV images for the cross-correlation algorithm, and additional artificial particles were not needed. This also reduced the possibility of the light scattered off seeded particles distorting the PLIF measurements. The PIV images were processed using the PIVsuite package developed by Jiri Vejrazka in MATLAB, implementing a multi-pass interrogation with final window size 24×24 pixels (0.78mm×0.78mm).

4. Planar laser induced fluorescence (PLIF)

Rhodamine 6G was chosen as the fluorescent dye to act as a scalar tracer in the PLIF measurements. This has a high absorption near the laser wavelength of 532nm and peak emission at approximately 560nm (Zehentbauer et al., 2014). The Rhodamine 6G concentrations used in the sourced mixture were in the range 40ppb $\lesssim K_0 \lesssim$ 160ppb, with the higher concentrations corresponding to experiments where the region of interest was further downstream from the inlet, after the jet had undergone considerable mixing/diluting. The concentration in the region of interest was typically $K \lesssim$ 20ppb, well within the linear excitation range reported by Zehentbauer et al. (2014), and confirmed by our own measurements. A B+W Orange MRC 040M filter was used on the PLIF cameras to cut off light below approximately 550nm, allowing the fluorescence from the dye, but not the scattered light from the particles, through to the CCD sensor.

4.1. Laser power correction

Although the present Nd:YAG laser is capable of operating at high frequency and power, the power output and profile shape of the beam can vary up to 5%

between individual pulses. To account for this variation, an additional camera was used to capture the fluorescence of a uniform water and Rhodamine 6G mixture before it reaches the region of interest. The mixture sits inside the 'laser calibration box' shown in figure 1, which is fitted with anti-reflective coated optical glass and placed in the path of the laser sheet outside of the main tank. The captured image of the fluoresced fluid is then a measurement of the laser power profile of that pulse. Images captured of the fluid in the laser calibration box will be denoted I_p, while images of the region of interest denoted, I. The box contained approximately 1L of the water with a typical Rhodamine concentration of 15ppb. It was observed that the pixel intensities in I_p would gradually decrease after several hundred images/laser pulses, which was attributed to some percentage of the dye particles in the box photobleaching and losing their fluorescence, thus reducing the overall signal. This effect was negligible within the maximum number of images of a single run ($\lesssim 400$), but could be detected after several runs (e.g. $\gtrsim 1200$ images). To prevent this effect, and thus maintain reliable power measurements, the box was re-filled with a fresh (unbleached) Rhodamine 6G mixture after each run. With a measurement of the power profile of the laser sheet for any individual pulse, the corresponding PLIF images in the region of interest could be corrected so that differences in the profile (in both magnitude and shape) between pulses were accounted for. After this correction, the PLIF images were filtered using a wavelet based denoising algorithm designed for CCD cameras (Weinkauff et al., 2015).

4.2. Image processing algorithm

The PLIF image processing procedure can be summarised by equations 2-4. Equation 4 corresponds to the final processing method used, and 2 and 3 are methods that were tested for validation purposes.

i. Standard method.

$$C = \frac{I - I_b}{\hat{I}_c} \tag{2}$$

ii. Power profile corrected.

$$C = \frac{(I - I_b)/P}{\tilde{I}_c} \tag{3}$$

iii. Power profile corrected and images denoised with wavelet filter.

$$C = \frac{\mathcal{D}\{(I - I_b)/P\}}{\mathcal{D}\{\tilde{I}_c\}} \tag{4}$$

Here I corresponds to the raw PLIF image of the region of interest taken during an experiment, I_b is a background image capturing any ambient light present, and $\hat{I}_c$ and $\tilde{I}_c$ are reference images corresponding to the maximum possible Rhodamine concentration in the tank. Images I_b, $\hat{I}_c$ and $\tilde{I}_c$, and the procedures for generating them, are discussed further in section 4.3 and 4.4. These images can be used to calculate the scalar concentration, C, in the region of interest through equation 2 (Shan et al., 2004; Crimaldi, 2008; Williamson et al., 2018), which assumes variations in the laser power profile are negligible between pulses. Equation 3 omits this assumption by including the laser power profile, P, which corresponds to the PLIF images I. The third method, equation 4, additionally includes applying the wavelet-based denoising filter (Weinkauff et al., 2015), denoted here by $\mathcal{D}\{\cdot\}$. All three methods rely on weak absorption (valid for low dye concentrations), and assume that light attenuation along the laser path is similar in I, $\hat{I}_c$ and $\tilde{I}_c$ (Shan et al., 2004), which is discussed further in §4.4. It additionally assumes that lens vignetting effects are the same in I, $\hat{I}$ and I_b (Ferrier et al., 1993).

In order to obtain the one-dimensional power profile, P, the image taken of the laser calibration box fluid, I_p, needed to be mapped to a one-dimensional vector with matching vertical world-coordinates to the main PLIF image, I. Any small misalignment of the laser optics could cause the laser sheet to widen/contract or shift vertically between the laser calibration box and the region of interest in the tank, which could result in I and P being vertically misaligned. This effect is negligible within the region of interest of I (width $\lesssim$ 120mm), but may not be in the distance between the region of interest and the laser calibration box (approximately 800mm). To account for this, and to ensure P is correctly aligned with I, an additional set of reference images were taken where a small vertical section of the laser sheet was obstructed by a cable. The location of the intensity dip in I_p and I was then matched so that the one-dimensional power profile

extracted from I_p could be interpolated to exactly match the world-coordinates of the laser sheet appearing in I. This procedure allows the laser power profile, P, to be calculated from equation 5,

$$P = \mathcal{M}\left\{\overline{I_p}\right\}, \tag{5}$$

where $\overline{I_p}$ denotes the mean column in image I_p, and $\mathcal{M}\{\cdot\}$ represents mapping the world coordinates to ensure P and I are correctly aligned.

This PLIF processing procedure was validated by taking 100 images of the tank containing fluid of a known concentration (defining this as $C = 1$), and running it through the three processing methods given in equations 2-4 to compute the concentration field. The difference between the calculated concentration and the actual concentration is then the error. The results of this validation are presented in figure 2, which shows the mean spectra of the error in a single column of the images. This was computed by taking the Fourier transform of the error in this column in every image, and then calculating the mean. The $\circ$ and $\triangle$ markers in figure 2 show that the error at low to medium frequencies is reduced when the power correction is applied (method (ii) versus (i)), but that there is little effect at high frequencies. This corresponds to reducing the error due to variations in both the mean power and the profile shape between pulses, without having a significant effect on the high frequency noise. Conversely, when the denoising filter is applied, it does not significantly affect the lower frequencies but reduces the error in the high frequency noise. Method (iii), applying both the power profile correction and denoising filter, was therefore used in calculating the concentration field from the PLIF measurements.

4.3. Background image

To account for the camera's black level and any ambient background light present in the experiments, a background image, I_b, without any flow present was taken so that it could be subtracted from the experimental images, I. However, due to the experimental procedure used in the present study, two background images were taken, $I_{b,0}$ and $I_{b,end}$ (one before the experiment and one at

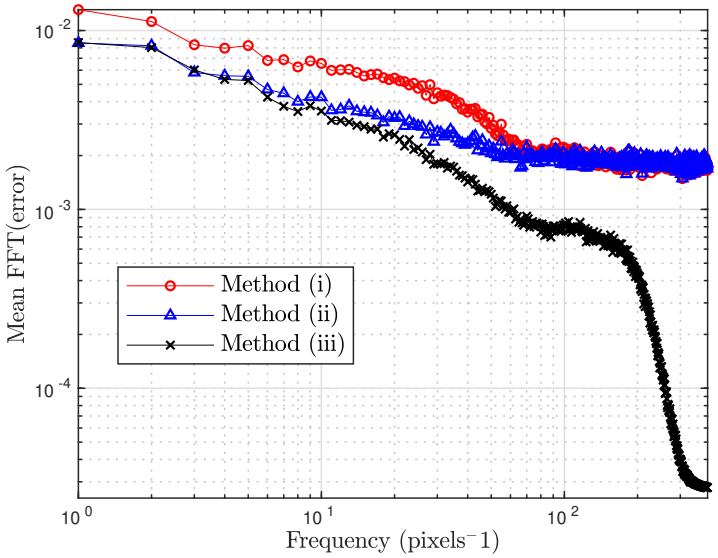

Figure 2: The spectra of the error in scalar concentration measurements produced from the three different PLIF processing methods described in equations 2-4. The ∘ markers correspond to the 'standard' method (i) without any laser profile correction or denoising, the △ to when only the profile correction is applied (ii), and the × for when both the profile correction and denoiser is applied (iii).

the end). This is because in order to capture sufficiently many images to obtain statistical convergence, each experiment consisted of multiple 'runs' that would linearly increase the background signal. Each run involved operating the pump for a fixed length of time (typically between 15 to 130s) using the pump's timing mode. This would add a known volume of source fluid to the tank each run, slightly changing the ambient fluid's density and Rhodamine 6G concentration. Because of the short experimental time and large tank volume relative to source fluid, after stirring around the tank the ambient fluid density would change by $\lesssim 0.008\%$ and Rhodamine concentration by $\lesssim 0.4$ppb each run. The change in density has a negligible effect on the source Froude and Reynolds numbers, and so is assumed to have a negligible effect on the flow dynamics. However, the increasing concentration of Rhodamine 6G dye in the ambient can be detected as a linearly increasing background signal in the PLIF images. This effect is

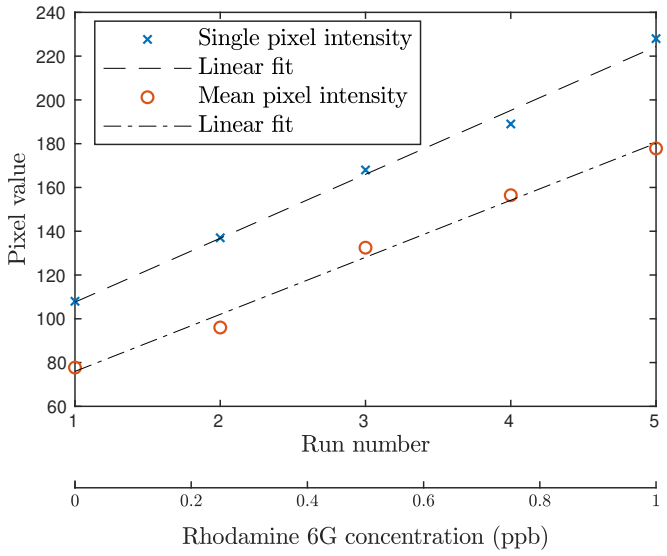

Figure 3: The intensity value (count) of a single pixel, and mean of all the pixels, in several background images taken prior to each run during an experiment. A small, fixed, amount of Rhodamine 6G is added to the ambient during each run, and so the background signal grows linearly.

accounted for by linearly interpolating between $I_{b,0}$ and $I_{b,end}$ to create an image, I_b, for each run in the experiment. This procedure was validated during an experiment in which background images were taken prior to each run so that the growing pixel intensity could be recorded and confirmed to be linear. Figure 3 shows the value of both a single pixel and the mean of all the pixels in these background images with each run, with a second axis also indicating the Rhodamine 6G concentration in the tank at the time. The trend is linear, and thus it was considered sufficient to take background images only at the start and end of the experiment, $I_{b,0}$ and $I_{b,end}$, and interpolate between them to obtain I_b for each run.

4.4. Calibration reference image

The PLIF algorithm described by equations 2-4 requires the reference images, $\hat{I}_c$ and $\tilde{I}_c$, which are obtained by taking 100 images of the tank filled with fluid with a constant Rhodamine 6G concentration, typically $K_c \cong 5$ppb, and

applying equations 6 and 7.

$$\hat{I}_c = \langle I_c - I_{b,0} \rangle \frac{K_0}{K_c} \tag{6}$$

$$\tilde{I}_c = \langle (I_c - I_{b,0})/P_c \rangle \frac{K_0}{K_c} \tag{7}$$

Here I_c is a single image of the tank containing fluid with uniform Rhodamine concentration K_c, the corresponding laser profile is P_c, and the angle brackets denote averaging over all 100 images. The Rhodamine 6G concentration of the source mixture, typically between 40 and 160ppb, is denoted by K_0. Images $\hat{I}_c$ and $\tilde{I}_c$ are then reference images that correspond to a maximum scalar concentration of $C = 1$, where $\tilde{I}_c$ employs the laser profile correction on each image in the ensemble and $\hat{I}_c$ does not.

During experiments, the PLIF cameras are focused near the centre of the 1m^3 tank where the flow is, meaning the laser sheet travels through approximately 500mm of ambient fluid before it enters the region of interest. There will be some light attenuation of the laser sheet along this path, so there will be less laser light in the region of interest than the laser calibration box. There will also be slightly less laser light available in the left side of the images than than the right side as the sheet attenuates light within the region of interest. This light attenuation in the laser path is accounted for in the reference images, $\hat{I}_c$ and $\tilde{I}_c$, as they will be subject to a similar attenuation effect as the PLIF images, I. The attenuation will not be exactly the same since in $\hat{I}_c$ and $\tilde{I}_c$ the laser sheet travels through the ambient with a uniform Rhodamine concentration of $K_c \cong 5$ppb, while during experiments the Rhodamine concentration will not be uniform (it will be highest along the jet centreline and low further from the jet). The difference in attenuation in these two cases is assumed to be negligible, and so when the experimental images are divided by $\tilde{I}_c$, the intensity differences as a result of light attenuation approximately cancel out.

5. Negatively buoyant jet stage

As discussed in §1, a turbulent jet with negative buoyancy undergoes two distinct flow stages, an initial 'negatively buoyant jet' stage and a 'fully developed fountain' stage. The negatively buoyant jet stage consists of decelerating fluid moving towards its initial height, z_i, before it reverses direction and forms a return flow. The return flow then continues to develop, interacting with the inner flow, until it reaches a quasi-steady state when it can be considered a fully developed fountain, with its maximum height oscillating around z_{ss}. In order to define the negatively buoyant jet stage of this inherently transient flow, an ensemble average is taken across multiple experimental runs with the same source conditions running for the same amount of time. For example, a $Fr_o = 30$ negatively buoyant jet would be imaged for 133.33s at 3Hz (400 images) in a single run, which would then be repeated 6 times (2400 images in total). An ensemble average for each time step would then be taken across the 6 runs so that there are 400 reasonably smooth 'averaged images' in time, which allows for the transient development of the negatively buoyant jet into a fully developed fountain to be investigated. This can be quantified by calculating the instantaneous volume flux, Q, at each time-step, but corresponding to the inner and outer flow separately, Q_{IF} and Q_{OF}, and observing how this changes in time. For simplicity, the boundary between the IF and OF is defined as the radial location, r_i, where the mean velocity profile of the fully developed fountain is first equal to zero. Although the actual instantaneous IF/OF boundary is likely to change in time as a negatively buoyant jet evolves into a fountain, r_i will be taken as fixed for the purposes of calculating Q_{IF} and Q_{OF}. That is,

$$Q_{IF} = 2\int_0^{r_i} \tilde{U} r \mathrm{d}r, \quad Q_{OF} = 2\int_{r_i}^{\infty} \tilde{U} r \mathrm{d}r, \qquad (8a-b)$$

where $\tilde{U}$ is the instantaneous velocity profile obtained after an ensemble average using profiles from several runs corresponding to the same instant in time. The ratio $-Q_{OF}/Q_{IF}$ is then plotted against time in figure 4 for a $Fr_o = 30$ negatively buoyant jet at distance $z/D \cong 18$ from the source.

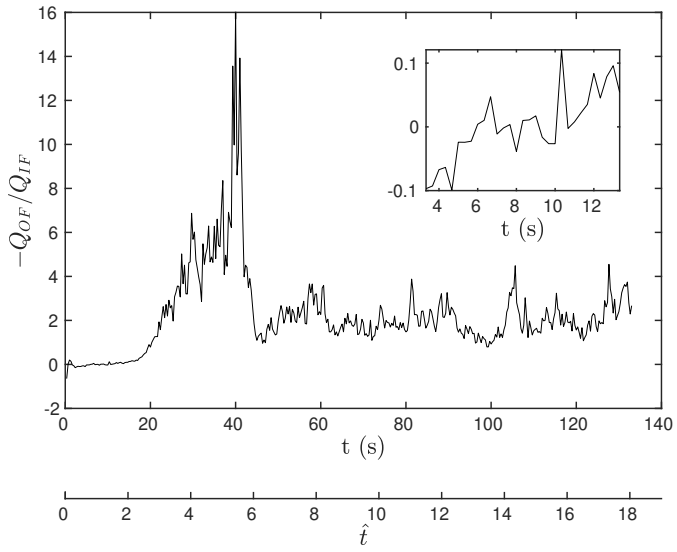

Figure 4: The time-development of ratio $-Q_{OF}/Q_{IF}$ in a $Fr_o = 30$ negatively buoyant jet, based on an ensemble average of 6 runs each long enough to capture the development to a fully developed fountain. The upper horizontal axis, t, is dimensional time in seconds. The lower axis $\hat{t} = tb_o/U_o$ is a non-dimensional time scale based on the source parameters. For this experiment, $b_o = 95.9\text{mm/s}^2$ and $U_o = 657\text{mm/s}$. Part of the plot has been enlarged and is shown in the upper right corner of the figure.

There are three notably distinct regions in figure 4, the first when $-Q_{OF}/Q_{IF} \cong 0$ ($\hat{t} \cong 0.5 - 1.9$), which is also shown in the enlarged section of the figure. Although the ratio appears to slightly increase across this range, this is considered negligible compared to the subsequent transient behaviour observed, and so $-Q_{OF}/Q_{IF}$ is considered approximately constant here. The ratio then rapidly increases then decreases ($\hat{t} \cong 1.9 - 6.4$), before it finally oscillates around a relatively constant value of $-Q_{OF}/Q_{IF} \cong 2$ ($\hat{t} \gtrsim 6.4$). The first stage has a small and approximately constant ratio where $-Q_{OF} << Q_{IF}$, indicating there is no significant flow in the outer region opposing the jet motion since the return flow has not yet established. After this, the ratio increases rapidly as $-Q_{OF}$ and Q_{IF} increase and decrease simultaneously, as fluid increasingly peels off the main jet and a return flow starts to form. The inner and outer flow continue

to interact, resulting in $-Q_{OF}/Q_{IF}$ decreasing to a quasi-steady equilibrium where it oscillates around a constant value and the fountain can be considered fully developed. Burridge and Hunt (2012) also reported on the transient behaviour of a developing fountain ($Fr_o = 11.8$), where it is indicated in their figure 13 that a return flow began to form at $\hat{t} \cong 1.3$, prior to the initial height being reached. This is in reasonable agreement with the end of the constant $-Q_{OF}/Q_{IF}$ stage in the present experiment (up to $\hat{t} \cong 1.9$), prior to the return flow forming. This stage will therefore be regarded as the negatively buoyant jet stage of the flow, and all time-averaged statistics presented will correspond to the initial stage where $-Q_{OF}/Q_{IF}$ is approximately constant. The fully developed fountain stage is taken to be the third stage of figure 4 ($\hat{t} \gtrsim 6.4$), after the transient region, where the ratio oscillates around $-Q_{OF}/Q_{IF} \cong 2$. Although figure 4 was produced by defining the IF/OF boundary, r_i, as the radial location where $\overline{U} = 0$ for the fully developed fountain ($t \cong 50 - 133$s), which seems to require a priori knowledge of when the fountain stage starts, the shape of the curve was found to be insensitive to the choice of r_i. The 'boundary' could also be defined as the half-width of the fountain velocity profile, or instead be based on an average of all the images, for example. The shape of $-Q_{OF}/Q_{IF}$ with time, and times of the different flow stages identified, remain approximately the same. This procedure is therefore adopted for all negatively buoyant experiments discussed in this investigation.

5.1. Mean profiles in time

After taking the ensemble average across multiple runs of the $Fr_o = 30$ negatively buoyant jet (same as that shown in figure 4), time-averaged profiles over several short time intervals (3.67s or 11 'images') were calculated for both the velocity and scalar measurements. These profiles are presented in figures 5 and 6 to illustrate the initially steady and then transient behaviour of the negatively buoyant jet as it develops into a fountain. The first three curves show averages taken over images $N = 10-20$, $20-30$ and $30-40$, which are all within the defined negatively buoyant jet range. The velocity and scalar profiles

are all very similar within this range, with no clear systematic trend in time. There are minimal negative values present in the velocity profiles in this range, indicating there is no return flow present. Beyond this point, for the profiles corresponding to images in the range $N = 40 - 70$, noticeable transient effects are observed in both the velocity and scalar profiles. In the velocity profiles, larger negative velocities are observed at the tail of the profile indicating a return flow starting to form. The scalar profiles are also changing strongly with time in this range, with an increasing peak concentration at the centreline, as well as higher values at the tails.

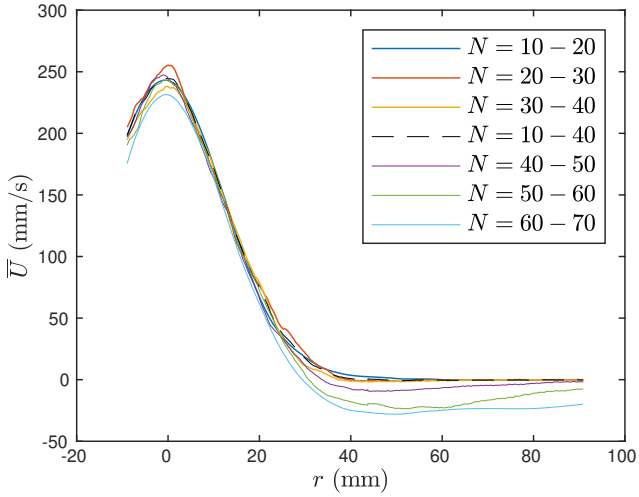

Figure 5: Mean axial velocity profiles of a negatively buoyant jet/fountain at various stages in time. The means are taken over 3.67s increments (corresponding to 11 'images' in time), in order to show how the velocity profiles change in time as the negatively buoyant jet develops into a fountain.

6. Results

PIV and LIF measurements are presented for neutrally buoyant jets of $Re_o \cong 10,000$ and $Re_o \cong 5900$, obtained using $D = 5$mm and $D = 10$mm pipes respectively, and a negatively buoyant jet (both start up and fully developed stages) with $Re_o \cong 5900$ and $Fr_o \cong 30$ using the $D = 10$mm pipe. Here the

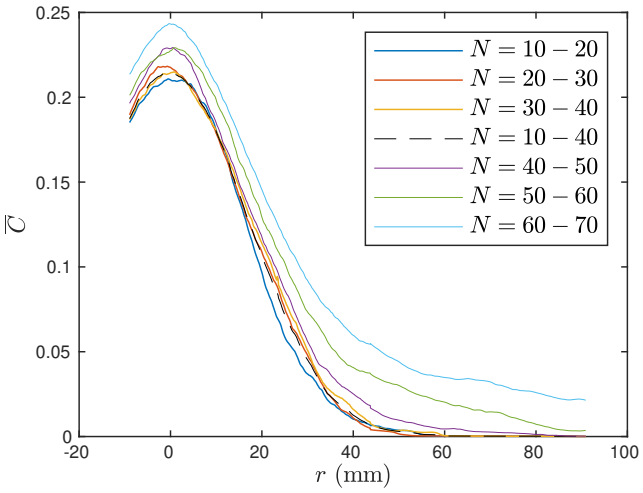

Figure 6: Mean scalar profiles of a negatively buoyant jet/fountain at various stages in time, using the same procedure as in figure 5.

source Reynolds number is defined as $Re_o = U_o D/\nu_o$, with ν_o representing the kinematic viscosity of the source mixture. The initial and steady state heights of the negatively buoyant jet/fountain at this Froude number are $z_i \cong 530$mm ($z/D \cong 53$) and $z_{ss} \cong 365$mm ($z/D \cong 37$). The mean axial velocity, $\overline{U}$, and scalar concentration, $\overline{C}$, profiles are shown in figures 7 and 8, along with data for a neutral jet from Wang and Law (2002), Darisse et al. (2015) and Webster et al. (2001). The horizontal axes have been normalised by the velocity and concentration profiles half-width, $r_{1/2,u}$ and $r_{1/2,c}$, respectively. This is defined as the radial distance where the velocity/concentration is equal to half that at the centreline. The vertical axes have been normalised by the value at the centreline.

The present velocity results in figure 7 for the neutral jet show good agreement with Wang and Law (2002), who also used freshwater/salt-water with a round inlet, as well as with Darisse et al. (2015) who used a contraction inlet to produce an air jet. The velocity profiles for the negatively buoyant jet and fully developed fountain are similar to the neutral jet for $r/r_{1/2,u} \lesssim 1.5$, with the fully developed case diverging beyond this point. This difference for the fully

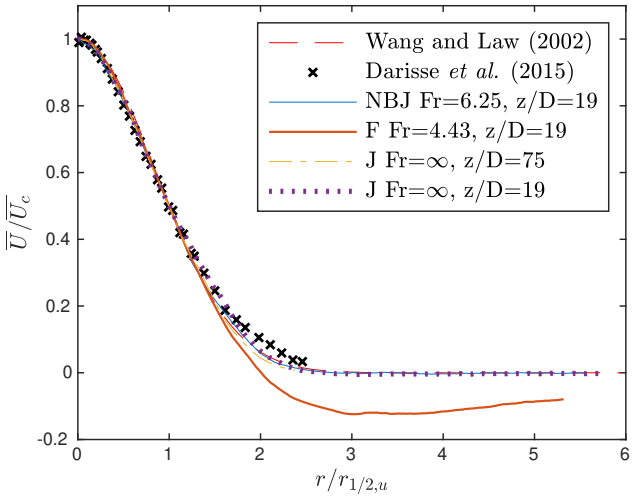

Figure 7: Velocity profiles from the present experiments for two neutral jets, J, ($Re_o \cong 10,000$ at $z/D = 73$ and $Re_o \cong 5900$ at $z/D = 19$), a negatively buoyant jet, NBJ, and a fully developed fountain, F, (both $Re_o \cong 5900$ and $Fr_o \cong 30$). Experimental data from Darisse et al. (2015) and the Gaussian fit from Wang and Law's (2002) results are also shown.

developed fountain is expected, with negative velocities seen after $r/r_{1/2,u} \cong 2.0$ corresponding to the return flow. The differences between the fountain and the other cases in the region $1.5 \lesssim r/r_{1/2,u} \lesssim 2.0$ indicates this is where the inner jet-like flow and return flow are interacting, reducing the inner flow velocity.

The present scalar concentration measurements are given in figure 8, with the neutral jet showing very close agreement with Wang and Law (2002) and Webster et al. (2001). The negatively buoyant jet profile is similar to the neutral case for most of its width. The fountain, however, has much higher concentrations further from the centreline (past $r/r_{1/2,c} \cong 1.0$, or in terms of velocity width, $r/r_{1/2,u} \cong 1.9$), reflecting the much wider scalar profile. This is consistent with the velocity measurements that also show the fountain profiles diverging from the negatively buoyant jet near this radial distance, likely due to interactions between the inner and outer flow that are not present in the negatively buoyant jet stage.

Figures 9(a)-(c) show the mean squared velocity fluctuations in the axial and

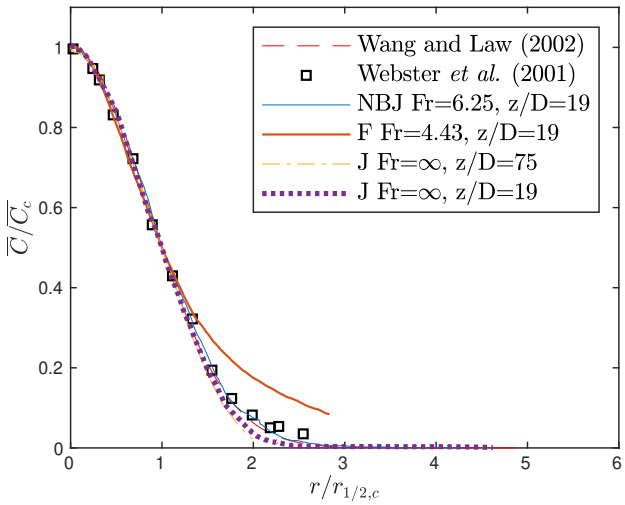

Figure 8: Scalar concentration profiles from the present experiments for two neutral jets ($Re_o \cong 10,000$ at $z/D = 73$ and $Re_o \cong 5900$ at $z/D = 19$), a negatively buoyant jet and a fully developed fountain (both $Re_o \cong 5900$ and $Fr_o \cong 30$). Neutral jet results from Webster et al. (2001) and the Gaussian fit from Wang and Law's (2002) data are also shown.

radial directions, $\overline{u'^2}$ and $\overline{v'^2}$, and the Reynolds stress, $\overline{u'v'}$, from the present PIV measurements. The neutral jet with $Re_o \cong 10,000$ at $z/D = 73$ is in very good agreement with Darisse et al. (2015) for $\overline{u'^2}$, $\overline{v'^2}$ and $\overline{u'v'}$, although the values for the $Re_o \cong 5900$ jet at $z/D = 19$ are somewhat lower. This may imply that the jet has not yet fully developed at this axial location, although it is still useful to discuss since it can be directly compared to the negatively buoyant jet and fountain at the same location. The negatively buoyant jet, which also has the same Re_o, has very similar values to the neutral jet in all three plots. The fully developed fountain, however, shows considerably larger fluctuations and stresses throughout its width, including inside the inner jet-like region ($r/r_{1/2,u} \lesssim 1.5$). This implies that the turbulent mixing occurring at the inner-flow/outer-flow 'boundary' ($1.5 \lesssim r/r_{1/2} \lesssim 2.0$) still has a noticeable effect near the jet centre. The larger values for the fountain also reflect the reduced axial velocity at the centreline, since $\overline{u'^2}$, $\overline{v'^2}$ and $\overline{u'v'}$ are all normalised by $\overline{U_c}^2$ in these plots. The turbulent velocity fluctuations and Reynolds stress remain high, relative to the

centreline velocity, despite the inner-flow being slowed down due to the opposing outer-flow.

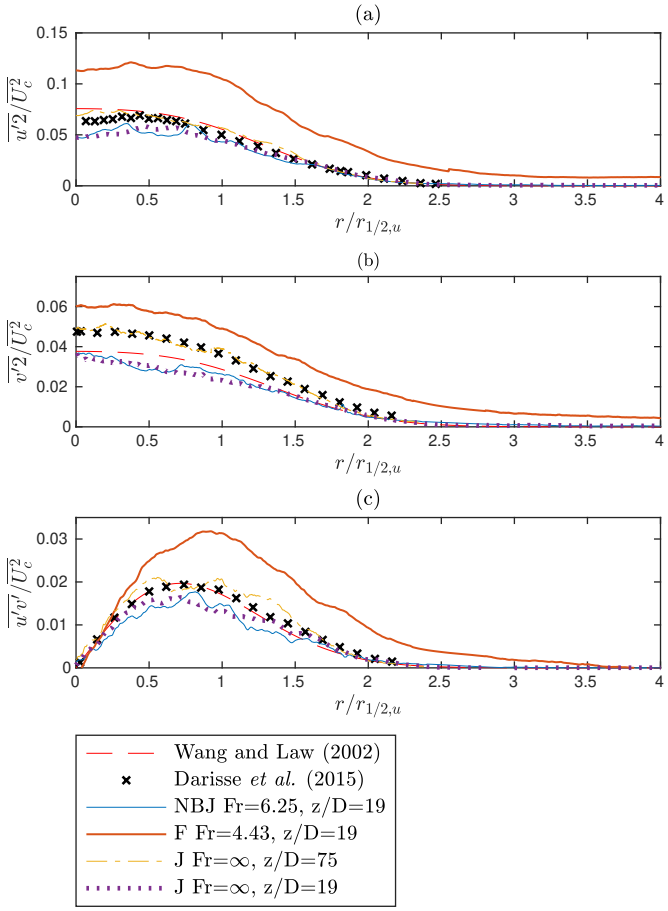

Figure 9: Present results for mean turbulent fluctuations and Reynolds stress for the same neutral jets, negatively buoyant jet and fountain as figures 7 and 8. Figure (a) shows the mean axial velocity fluctuations, $\overline{u'^2}$, (b) the radial fluctuations, $\overline{v'^2}$, and (c) the Reynolds stress, $\overline{u'v'}$. Neutral jet results from Wang and Law (2002) and Darisse et al. (2015) are also shown.

6.1. Entrainment

For a high Re_o axisymmetric jet or plume with arbitrary buoyancy, by invoking the Boussinesq approximation and the entrainment assumption, the following equation for conservation of volume flux can be derived (van Reeuwijk

α	Flow	Study
0.058	J	Present experiments
0.054	NBJ	Present experiments
0.057	J	Experiments (Ezzamel et al., 2015)
0.067	J	DNS (van Reeuwijk et al., 2016)

Table 1: The entrainment coefficient, α, for a neutral and negatively buoyant jet, as calculated using equation 9. The values of α estimated for neutral jet by Ezzamel et al. (2015) and van Reeuwijk et al. (2016) are also given.

and Craske, 2015),

$$\frac{\mathrm{d}Q}{\mathrm{d}z} = 2\alpha M^{1/2}. \tag{9}$$

Here Q and M are the volume and momentum flux defined below, and α is the entrainment coefficient.

$$Q = 2\int_0^\infty \overline{U} r \mathrm{d}r \tag{10}$$

$$M = 2\int_0^\infty \overline{U}^2 r \mathrm{d}r \tag{11}$$

A direct calculation of α from equation 9 may therefore be performed using the mean velocity field obtained from the PIV measurements. This procedure for calculating α is valid for the initial negatively buoyant jet stage of the flow, as well as for neutral jets. To avoid scatter in $\mathrm{d}Q/\mathrm{d}z$, due to the spatially discrete velocity data, a linear fit of Q was taken. Although it is unlikely that $Q(z)$ will be linear for the entire of the length of the negatively buoyant jet, it was found to be a reasonable approximation within the region of interest of the present experiments ($17 \lesssim z/D \lesssim 20$).

The calculated α for a neutral and negatively buoyant jet are given in table 1, along with estimates by Ezzamel et al. (2015) and van Reeuwijk et al. (2016) for a neutral jet. The present results give an estimate of $\alpha \cong 0.058$ for a neutral jet, and $\alpha \cong 0.054$ for a negatively buoyant jet over the region of interest investigated. The measured α for a neutral jet is somewhat lower than the

estimate by van Reeuwijk et al. (2016) of $\alpha = 0.067$, but very similar to the average value of Ezzamel et al.'s (2015) data, $\alpha = 0.057$ (from their figure 18), at a similar downstream location. The α measurement for the negatively buoyant jet is lower than the neutral jet values, which is consistent with the conclusions of Papanicolaou et al. (2008) and Pantzlaff and Lueptow (1999), who suggested that the entrainment coefficient is reduced in jets with negatively buoyancy.

6.2. Uncertainty

Determining the uncertainty of the present α value requires knowledge of the uncertainty of the mean axial velocity profile, $\overline{U}$. This is given by (Wilson and Smith, 2013a,b),

$$U_{\overline{U}} = \sqrt{\langle b_{U_i} \rangle^2 + p_{\overline{U}}^2} \tag{12}$$

where $\langle b_{U_i} \rangle$ is the average of the systematic or bias errors in the instantaneous velocity fields, U_i, and $p_{\overline{U}}$ is the precision uncertainty due to the finite number of samples (images),

$$p_{\overline{U}} = \pm k \frac{s_U}{\sqrt{N_t}}. \tag{13}$$

Here $s_{\overline{U}}$ is the standard deviation of the samples, N_t is the total number of samples, and k is a constant that determines the confidence interval. For a 95% confidence interval assuming a normally distributed error, $k = 1.96$ (Wilson and Smith, 2013a; Coleman and Steele, 2018). For the present velocity measurements, $s_{\overline{U}}$ is taken as the maximum value of $\sqrt{\overline{u'^2}}$ at $z/D = 19$. This corresponds to the square root of maximum value of the curves in figure $9(a)$, except the dimensional (non-normalised) value is used. For the neutral and negatively buoyant jets, $P_{\overline{U}} \cong \pm 2.07$mm/s and $P_{\overline{U}} \cong \pm 3.69$mm/s, respectively. The uncertainty is lower in the neutral jet since it was possible to capture more images of the flow.

To estimate the systematic uncertainty in the instantaneous velocity fields obtained from the PIV algorithm, the 'image matching' method developed by Sciacchitano et al. (2013) is used. This method involves using the displacement

vectors for a single pair of images to deform and 'match' the two images. If the PIV algorithm was perfect, the two deformed images would exactly match, however in practice there is a disparity between the particle locations in the two images, which is used to estimate the error. This approach allows the random and systematic error to be estimated separately for each interrogation window in the image, but for the purposes of estimating $U_{\overline{U}}$, only the systematic error is needed. Applying this method to a number of image pairs from the present experiments found that the average systematic error in each instantaneous velocity field was $\lesssim 0.005$ pixels/time-step ($\lesssim 10^{-4}$mm/s), and so was assumed to be negligible. In this case, $\langle b_{U_i} \rangle \cong 0$ and the uncertainty of the mean velocity is equal to the precision uncertainty, $U_{\overline{U}} = p_{\overline{U}}$ (Sciacchitano and Wieneke, 2016).

To estimate the uncertainty of α, which was found using equation 9, approximate upper and lower bounds for M and $\mathrm{d}Q/\mathrm{d}z$ were calculated. For M, these were obtained using equations 14(a-b),

$$M_{up} = 2\int_0^\infty \left(\overline{U} + U_{\overline{U}}\right)^2 r\mathrm{d}r, \quad M_{low} = 2\int_0^\infty \left(\overline{U} - U_{\overline{U}}\right)^2 r\mathrm{d}r. \qquad (14a-b)$$

Since $\mathrm{d}Q/\mathrm{d}z$ was estimated using a linear fit of $Q(z)$, the 95% confidence interval of the linear coefficient of the fit was used to approximate the upper and lower bounds of $\mathrm{d}Q/\mathrm{d}z$. The uncertainty of α was then estimated, giving $\alpha = 0.058 \pm 0.0015$ ($0.056 \lesssim \alpha \lesssim 0.059$) and $\alpha = 0.054 \pm 0.0027$ ($0.052 \lesssim \alpha \lesssim 0.057$) for the neutral and negatively buoyant jets, respectively. Although there is an overlap in the uncertainty ranges for the J and NBJ, meaning it is possible that the difference is due to experimental error, the overlap is reasonably small and it is suggested that the lower entrainment in the NBJ is a genuine result, consistent with existing literature (Pantzlaff and Lueptow, 1999; Papanicolaou et al., 2008).

7. Conclusions

PIV and PLIF measurements have been presented for a neutral jet, negatively buoyant start-up jet and fully developed fountain. A correction procedure

for the PLIF measurements has been discussed, which accounts for variations in power magnitude and profile shape between laser pulses. This procedure has been demonstrated to reduce the error in the concentration field for the present Nd:YAG laser. The profiles for velocity, scalar concentration, turbulent fluctuations and Reynolds stress have been presented for all three jet cases. There are close similarities between all of these profiles for the neutral and negatively buoyant jet, when normalised by the centreline velocity, in the downstream range investigated ($17 \lesssim z/D \lesssim 20$). For a fully developed fountain, the mean velocity and scalar profiles are similar to the neutral and negatively buoyant jet in the inner-jet region ($r/r_{1/2,u} \lesssim 1.5$), but diverge further from the centreline where the inner and outer flow interact. The normalised turbulence quantities are much higher in the fountain, indicating that the presence of a return flow affects the inner jet even near the centreline. The entrainment coefficient has also been estimated for a negatively buoyant jet ($\alpha \cong 0.054$), providing further evidence that entrainment is lower in negatively buoyant jets compared to neutral jets.

8. Acknowledgements

The support of the Australian Research Council for this project is gratefully acknowledged. We would also like to acknowledge Krishna M. Talluru for his useful assistance during the experiments.

References

Bloomfield, L.J., Kerr, R.C., 2000. A theoretical model of a turbulent fountain. Journal of Fluid Mechanics 424, 197–216.

Burridge, H., Hunt, G., 2012. The rise heights of low-and high-Froude-number turbulent axisymmetric fountains. Journal of Fluid Mechanics 691, 392–416.

Carazzo, G., Kaminski, E., Tait, S., 2006. The route to self-similarity in turbulent jets and plumes. Journal of Fluid Mechanics 547, 137–148.

Coleman, H.W., Steele, W.G., 2018. Experimentation, validation, and uncertainty analysis for engineers. John Wiley & Sons.

Crimaldi, J., 2008. Planar laser induced fluorescence in aqueous flows. Experiments in fluids 44, 851–863.

Darisse, A., Lemay, J., Benaïssa, A., 2015. Budgets of turbulent kinetic energy, Reynolds stresses, variance of temperature fluctuations and turbulent heat fluxes in a round jet. Journal of Fluid Mechanics 774, 95–142.

Ezzamel, A., Salizzoni, P., Hunt, G.R., 2015. Dynamical variability of axisymmetric buoyant plumes. Journal of Fluid Mechanics 765, 576–611.

Ferrier, A., Funk, D., Roberts, P., 1993. Application of optical techniques to the study of plumes in stratified fluids. Dynamics of Atmospheres and Oceans 20, 155–183.

Fox, D.G., 1970. Forced plume in a stratified fluid. Journal of Geophysical Research 75, 6818–6835.

Hunt, G., Burridge, H., 2015. Fountains in industry and nature. Annual Review of Fluid Mechanics 47, 195–220.

Hussein, H.J., Capp, S.P., George, W.K., 1994. Velocity measurements in a high-Reynolds-number, momentum-conserving, axisymmetric, turbulent jet. Journal of Fluid Mechanics 258, 31–75.

Kaminski, E., Tait, S., Carazzo, G., 2005. Turbulent entrainment in jets with arbitrary buoyancy. Journal of Fluid Mechanics 526, 361–376.

McDougall, T.J., 1981. Negatively buoyant vertical jets. Tellus 33, 313–320.

Morton, B., Taylor, G.I., Turner, J.S., 1956. Turbulent gravitational convection from maintained and instantaneous sources. Proceedings of the Royal Society of London. Series A. Mathematical and Physical Sciences 234, 1–23.

Pantzlaff, L., Lueptow, R.M., 1999. Transient positively and negatively buoyant turbulent round jets. Experiments in Fluids 27, 117–125.

Papanicolaou, P.N., Papakonstantis, I.G., Christodoulou, G.C., 2008. On the entrainment coefficient in negatively buoyant jets. Journal of Fluid Mechanics 614, 447–470.

Priestley, C., Ball, F., 1955. Continuous convection from an isolated source of heat. Quarterly Journal of the Royal Meteorological Society 81, 144–157.

van Reeuwijk, M., Craske, J., 2015. Energy-consistent entrainment relations for jets and plumes. Journal of Fluid Mechanics 782, 333–355.

van Reeuwijk, M., Salizzoni, P., Hunt, G.R., Craske, J., 2016. Turbulent transport and entrainment in jets and plumes: A DNS study. Physical Review Fluids 1, 074301.

Sciacchitano, A., Wieneke, B., 2016. Piv uncertainty propagation. Measurement Science and Technology 27, 084006.

Sciacchitano, A., Wieneke, B., Scarano, F., 2013. PIV uncertainty quantification by image matching. Measurement Science and Technology 24, 045302.

Shan, J.W., Lang, D.B., Dimotakis, P.E., 2004. Scalar concentration measurements in liquid-phase flows with pulsed lasers. Experiments in Fluids 36, 268–273.

Wang, H., Law, A.W.K., 2002. Second-order integral model for a round turbulent buoyant jet. Journal of Fluid Mechanics 459, 397–428.

Webster, D.R., Roberts, P.J., Ra'ad, L., 2001. Simultaneous DPTV/PLIF measurements of a turbulent jet. Experiments in Fluids 30, 65–72.

Weinkauff, J., Trunk, P., Frank, J., Dunn, M., Dreizler, A., Böhm, B., 2015. Investigation of flame propagation in a partially premixed jet by high-speed-Stereo-PIV and acetone-PLIF. Proceedings of the Combustion Institute 35, 3773–3781.

Williamson, N., Kirkpatrick, M., Armfield, S., 2018. Entrainment across a sheared density interface in a cavity flow. Journal of Fluid Mechanics 835, 999–1021.

Wilson, B.M., Smith, B.L., 2013a. Taylor-series and Monte-Carlo-method uncertainty estimation of the width of a probability distribution based on varying bias and random error. Measurement Science and Technology 24, 035301.

Wilson, B.M., Smith, B.L., 2013b. Uncertainty on PIV mean and fluctuating velocity due to bias and random errors. Measurement Science and Technology 24, 035302.

Zehentbauer, F.M., Moretto, C., Stephen, R., Thevar, T., Gilchrist, J.R., Pokrajac, D., Richard, K.L., Kiefer, J., 2014. Fluorescence spectroscopy of Rhodamine 6G: concentration and solvent effects. Spectrochimica Acta Part A: Molecular and Biomolecular Spectroscopy 121, 147–151.